Controllable growth of MoS$_2$ nanosheets on novel Cu$_2$S snowflakes with high photocatalytic activity

Xinjie Zhang, Yichen Guo, Jian Tian*, Benteng Sun, Zhangqian Liang, Xuesong Xu, Hongzhi Cui*

School of Materials Science and Engineering, Shandong University of Science and Technology, Qingdao, 266590, China

ARTICLE INFO

ABSTRACT

Herein, we, for the first time, report the controllable syntheses of the snowflake-like Cu$_2$S architectures by using a template free, facile hydrothermal route, in which thiourea as the precursor of sulfur and EDA as the solvent. It is surprising that the Cu$_2$S snowflakes show a higher photocatalytic activity than the other samples (Cu$_2$S dendrites and sheets), has been mainly ascribed to its high light absorbance and BET area. Then the MoS$_2$ nanosheets (NSs) are uniformly distributed on the Cu$_2$S snowflake (SF) substrate, the obtained MoS$_2$ NS/Cu$_2$S SF composite manifests high specific surface area (60.512 m^2 g^{-1}) and large pore volume (0.148 cm^3 g^{-1}), which are favorable for the efficient light capturing together with the rapid transfer of charge carriers. In comparison with the pure Cu$_2$S, the MoS$_2$ NS/Cu$_2$S SF composite exhibits much enhanced activity and long-term stability towards the photocatalytic degradation of organic dye pollutants and hydrogen production. The improved photocatalytic activity could be owed to two aspects, namely the enhanced light trapping and scattering ability benefited from large specific area of unique snowflake-like structural features and improved charge separation activity of heterojunction between MoS$_2$ and Cu$_2$S.

1. Introduction

Semiconductor-based photocatalysis is a potential strategy to solve the problems concerning energy crisis and environmental contamination through photocatalytic water splitting to produce hydrogen and degradation of organic pollutants into CO$_2$ and H$_2$O [1]. Among various semiconductor photocatalysts, TiO$_2$ is currently one of the most extensively used due to its superior properties: high resistance to long-term stability against photo and chemical corrosion, low cost and nontoxicity [2]. However, the photocatalytic reaction using pure TiO$_2$ has been severely restricted by its two fundamental properties [3]. Firstly, the spectrum of TiO$_2$ can absorb is limited to UV region due to the wide bandgap (3.2 eV for anatase, 3.0 eV for rutile) and secondly the rapid recombination of photogenerated conduction band (CB) electrons and valence band (VB) holes [4]. To overcome the drawbacks of TiO$_2$, various strategies have been proposed such as such as varying the chemical composition with metal or non-metal doping, the deposition of narrow bandgap semiconductors (such as Ag$_2$O [5], CdSe [6], and ZnS [7]) and the use of co-catalysts (*e.g.* metal and metal oxide or sulfide nanostructures) [8]. Among these, the co-catalyst strategies have proven to be one of the most effective ways to improve the photocatalytic water splitting performance [9]. When the co-catalysts are combined with semiconductor photocatalysts, an appropriate

heterojunction can be formed between these materials, which can improve the separation of photogenerated electrons and holes [10]. Also, the use of co-catalysts can potentially lower the activation potentials for hydrogen (H$_2$) evolution reactions [11]. Consequently, the application of a suitable co-catalyst can significantly improve the photocatalytic properties [12].

Since the properties of materials are strongly dependent on their shape and size, significant progress has been made on the morphology control of materials [13]. Copper sulfides (Cu$_2$S), with a bulk band gap of 1.2 eV, is a well-known p-type semiconductors due to the stoichiometric deficiency of copper in the lattice, which have attracted considerable attention because of their broad applications in diverse fields including photocatalysis, solar cells, chemical sensing, and nanoscale switches [14]. Recently, Cu$_2$S nanocrystals with different morphologies, such as nanoplates [15], nanosheets [16], nanorods [17], nanoparticles [18], quantum dots [19], and 3D hierarchical microstructures [20], have been explored by some pioneers. On the nanoscale, snowflake-like architectures are a type of hyper-branched structure, which is generally formed by hierarchical self-assembly under non-equilibrium conditions. Another solution is to maximize the surface area by developing abundant active sites on the substrate to enhance light trapping and scattering capability [21]. Most recently, snowflake-like architectures have been reported with the purpose of ensuring high surface area to

---

reinforce light scattering and trapping in the application on solar cells [22]. The scrupulous design of these smart architectures is similar to the natural trees which possess of branched structures with stems and leaves [23,24]. In the literature, a variety of snowflake-like architectures have been fabricated, such as $BiPO_4$ [21], Fe_2O_3 [25], ZnO [26] and so on. However, snowflake-like Cu_2S architectures have been rarely reported.

Two-dimensional (2D) layered nanocrystals with ultra-thin thickness such as MoS_2 nanosheets (NSs), have gained extensive attention for their promising practical applications and theoretical values [27]. MoS_2 in the form of nanosheets usually exhibits much better catalytic performance due to its 2D layered structure with a larger surface area and more active sites than those of other nanostructures [28]. Furthermore, the layer of MoS_2 also governs its properties and performance, as both the active sites and adsorption ability are substantially influenced by the layered nanostructure [29]. To date, the MoS_2-based semiconductor heterostructures, such as CdS/MoS_2 [30], MoO_3/MoS_2 [31], SnO_2/MoS_2 [32], with good photocatalytic or photoelectrochemical properties have been successfully synthesized, since the efficient charge separation can be obtained by coupling two semiconductor structures with the matched energy levels. Thus, using 2D MoS_2 NSs is reasonable for strengthening the visible photocatalytic performance of Cu_2S.

Herein, we introduced ethylenediamine (EDA) as solvent and thiourea as the precursor of sulfur, and presented a hydrothermal strategy to synthesize novel Cu_2S snowflakes (SFs). A plausible branching growth mechanism has been proposed to understand the formation of Cu_2S SFs. To the best of our knowledge, this is the first report on the synthesis of Cu_2S SFs. During the synthesis process, EDA could serve as solvent-template, which guided the crystal growth direction of Cu_2S SFs. Then few-layers MoS_2 nanosheets (NSs) discontinuously are grown on Cu_2S SFs to construct MoS_2 NS/Cu_2S SF composites. The photocatalytic degradation experiments on methyl orange (MO) under visible light irradiation showed that the as-synthesized MoS_2 NS/Cu_2S SF composites possess high photodegradation efficiency toward organic dye molecules. Moreover, they could also act as effective cocatalysts for photocatalytic H_2 production, which greatly improved the H_2 production rate of TiO_2. Thanks to the unique snowflake-like architecture and heterojunction between MoS_2 and Cu_2S, The MoS_2 NS/Cu_2S SF composites obtain high solar energy capture efficiency and convenient charge transfer channels and thus exhibit high photocatalytic activities.

2. Experimental section

2.1. Materials

The chemicals used in this work were of analytical reagent grade. Thiourea ((NH_2)$_2$CS), ethylenediamine (EDA), copper chloride dihydrate ($CuCl_2 \cdot 2H_2O$), sodium molybdate dihydrate ($Na_2MoO_4 \cdot 2H_2O$), and silver nitrate ($AgNO_3$) were purchased from Sinopharm and used without further purification.

2.2. Preparation of Cu_2S architectures (dendrites, snowflakes and sheets)

The Cu_2S architectures were prepared by using a facile hydrothermal method. In a typical synthesis procedure, 1 mmol $CuCl_2 \cdot 2H_2O$ was dissolved in 30 mL EDA. To this, 3 mmol (NH_2)$_2$CS was added under constant magnetic stirring to ensure good dispersion of the reactants. After stirring for 2 h, the solution was put into a 50 mL Teflon-lined stainless steel autoclave and the temperature was maintained at 60 °C, 80 °C and 100 °C for 8 h. After cooling down, Cu_2S architectures were removed from the solution, washed thoroughly with distilled water and then with ethanol. Finally, the Cu_2S architectures (dendrites, snowflakes and sheets) were dried at 60 °C for 10 h in an oven for further characterization techniques.

2.3. Synthesis of MoS_2 nanosheet (NS)@Cu_2S snowflake (SF) composites

The formation process of MoS_2 NS@Cu_2S SF composites was described as follows. Typically, 6–18 mg $Na_2MoO_4 \cdot 2H_2O$ and 12–84 mg (NH_2)$_2$CS were dissolved in 20 mL deionized water to form a transparent solution, respectively. Then 50 mg Cu_2S snowflakes (SFs) powders (synthesized at 80 °C) were added into the above solution and stirred to form the suspension. The solution was transferred to Teflon-lined stainless steel autoclaves and then heated in an electric oven at 200 °C for 24 h. The MoS_2 NS@Cu_2S SF composites with different MoS_2 loading amounts: 30 wt%, 50 wt%, and 70 wt% were harvested after centrifugation and dried at 50 °C for 12 h.

2.4. Materials characterization

XRD pattern of samples were recorded on a Bruke D8 Advance powder X-ray diffractometer with Cu Kα (λ = 0.15406 nm). FEI NanoSEM 450 field-emission scanning electron microscope (FE-SEM) with an energy-dispersive X-ray spectroscopy (EDS) and JOEL JEM 2100 high resolution transmission electron microscope (HR-TEM) were used to characterize the morphologies of the catalysts. X-ray photoelectron spectroscopy (XPS) and Auger electron spectroscopy (AES) experiments were performed on a Thermo ESCALAB 250XI. UV–vis DRS of the catalysts were performed on a UV–vis spectrophotometer (Hitachi UV-3101). The specific surface area was calculated using the BET method and examined on a Micromeritics ASAP2020 instrument.

2.5. Photocatalytic activity test

The photocatalytic degradation performance of the samples was examined by the photodecomposition of methyl orange (MO, 20 mg/L). 20 mg of photocatalyst powders were added into 20 mL MO aqueous solutions in a 20 mL beaker, respectively. A 300 W Xe arc lamp with filter glasses to filter UV light were used as the visible light source. In a hydrogen evolution experiment, the MoS_2 NS@Cu_2S SF composite as co-catalysts (2.5 mg) and 47.5 mg TiO_2 were suspended in 100 mL water/methanol solution (mass ratio 80:20) with ultrasound for 1 h. A 300 W Xe arc lamp was used as the light source. The amount of H_2 evolved was performed on a Techcomp GC7900 gas chromatograph.

3. Results and discussion

3.1. Structure and morphology

In a typical synthesis of Cu_2S architectures (dendrites, snowflakes and sheets), $CuCl_2 \cdot 2H_2O$ and (NH_2)$_2$CS were used as copper and sulfur precursors, respectively, EDA was used as the solvent. The reaction was performed at 60–100 °C (for the detailed procedure, see the experimental section). Then few-layer MoS_2 nanosheets (NSs) discontinuously are grown on Cu_2S SFs to construct MoS_2 NS/Cu_2S SF composites (Scheme 1).

To control the morphology of nanomaterials, EDA had used as a classic bidentate ligand for its bonding nature with metal cations [33]. To understand the crystal growth behavior, temperature-dependent experiments in the presence of EDA were performed. The SEM images indicate the formation of snowflake-shaped Cu_2S architecture. At 60 °C (Fig. 1a), The Cu_2S is found to be made up of one or several dendrites. The SEM images (Fig. 1b and c) of the synthesized Cu_2S samples under 80 °C show that the samples are composed of snowflake structures. The unprecedented six-branch dendrites and further branching growth were achieved (Fig. 1b). This snowflake structure have six symmetrical oriented petals, and the length of six dendritic petals is about 3–4 μm. At the central position of the flower each dendritic petal of a flower-like dendrite merges with each other. It is noteworthy that some trunks have split into six to ten sub-branches (Fig. 1c). It is interesting that the intersection angles among the branches are 60° (Fig. 1c). Further
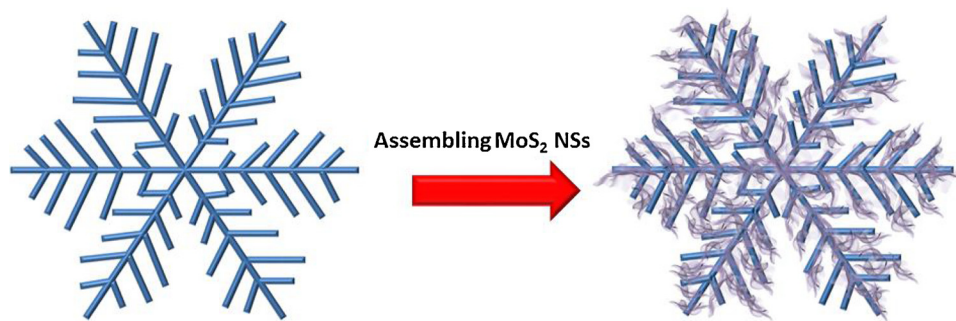
Scheme 1. Growth schematic of the as-synthesized MoS$_2$ NS/Cu$_2$S SF composites.

increasing the reaction temperature (100 °C), the interesting snowflake-like Cu$_2$S architectures are broken and the morphologies look like sheets (Fig. 1d). The significant differences in the Cu$_2$S morphologies at different reaction temperatures attributed to effective coordination degree of EDA. EDA can form the [Cu (En)$_2$]$^{2+}$ complex with the copper cation in the range of temperature 60–80 °C, which may first the nucleation and crystal growth of Cu$_2$S, and then formation of snowflake structures. Though, at higher reaction temperatures (100 °C), the solution will result in the form of the reduced complex due to the volatile nature of EDA. Consequently, the higher temperatures affect the morphology of the synthesized samples of Cu$_2$S. The energy-dispersive X-ray spectroscopy (EDS) mapping profiles of Cu$_2$S SFs synthesized under 80 °C, as shown in Fig. 2, obviously manifest the homogeneous distribution of Cu and S elements in Cu$_2$S SFs.

TEM images of Cu$_2$S SFs also confirm the regularity of snowflake architectures, as shown in Fig. 3a, which is well in conformity to SEM images (Fig. 1c). Fig. 3a shows clearly that snowflakes has a flat symmetrical structure with six oriented petals extending radially from the center button. It is noteworthy that some trunks have split into six to eight sub-branches as shown in Fig. 3a. Close examination of Cu$_2$S SFs with high-resolution TEM image (Fig. 3b) reveals that the Cu$_2$S architectures are single crystallites with a good crystallinity. The lattice

spacing of 0.189 nm, as shown in Fig. 3b, corresponds to the d spacing of the (573) plane of Cu$_2$S [34], which is consistent well with XRD result. These snowflake architectures can not only effectively enlarge the surface area, but also promote light scattering and thus resulting in an enhancement of photocatalytic performance.

The XRD patterns of the synthesized Cu$_2$S architectures under various reaction temperatures from 60 to 100 °C are shown in Fig. 4a–c. The positions of the diffraction peaks of samples match well with the theoretical values of orthorhombic Cu$_2$S phase (JCPDS 02-1294) [35]. The formation of Cu$_2$S phase is due to the reducing effect of EDA in the reaction medium. No other characteristic peaks from impurities, such as CuS, Cu$_{1.96}$S, Cu$_{1.8}$S, were detected, which revealed that the purity of the product was pretty high. Furthermore, the intensity and the sharp diffraction peaks suggested that the as-prepared Cu$_2$S was well crystallized and thus reduced electron transport resistance. As shown in Figs. 4d and S1, all intense and distinct peaks in the patterns of MoS$_2$ NS/Cu$_2$S SF composites with different MoS$_2$ loading amounts (30 wt%, 50 wt%, 70 wt% MoS$_2$) can be ascribed to hexagonal MoS$_2$ (JCPDS 37-1942) [27] and orthorhombic Cu$_2$S (JCPDS 02-1294), indicating that the MoS$_2$ NS/Cu$_2$S SF composites are successfully obtained. Besides, it seems that the peak intensities of MoS$_2$ increase (Fig. S1) constantly as the MoS$_2$ loading amounts grow.
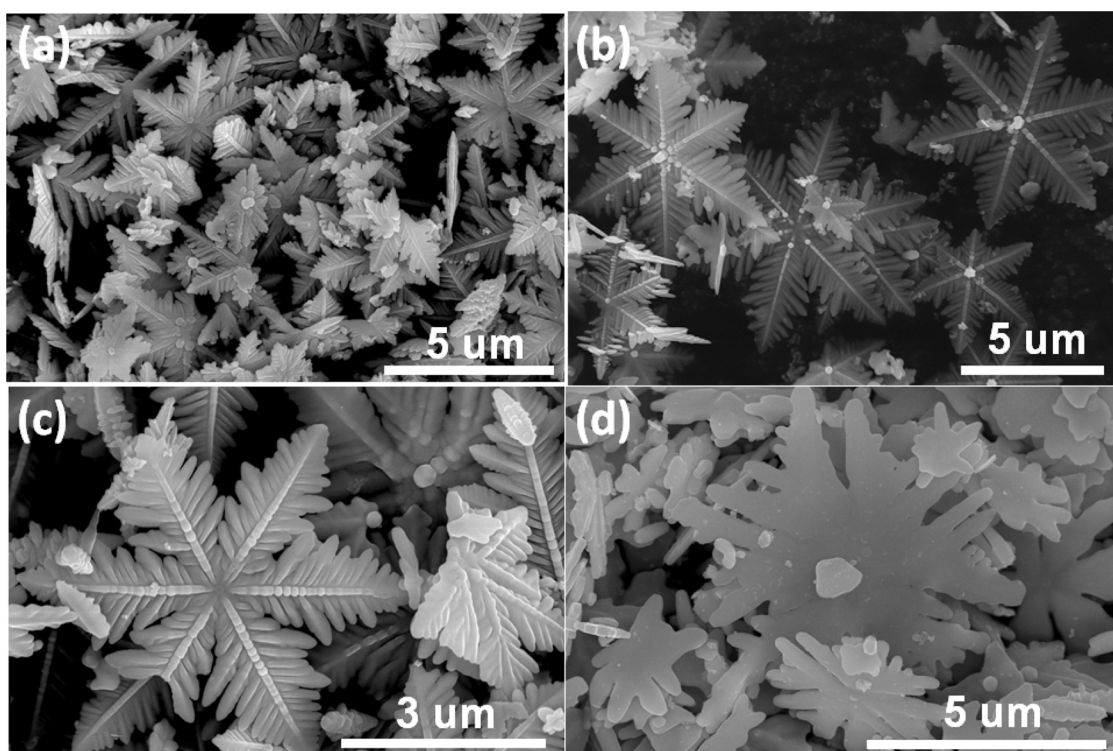
Fig. 1. SEM images of Cu$_2$S architectures synthesized under various reaction temperatures: (a) 60 °C (dendrites), (b, c) 80 °C (snowflakes), (c) 100 °C (sheets).
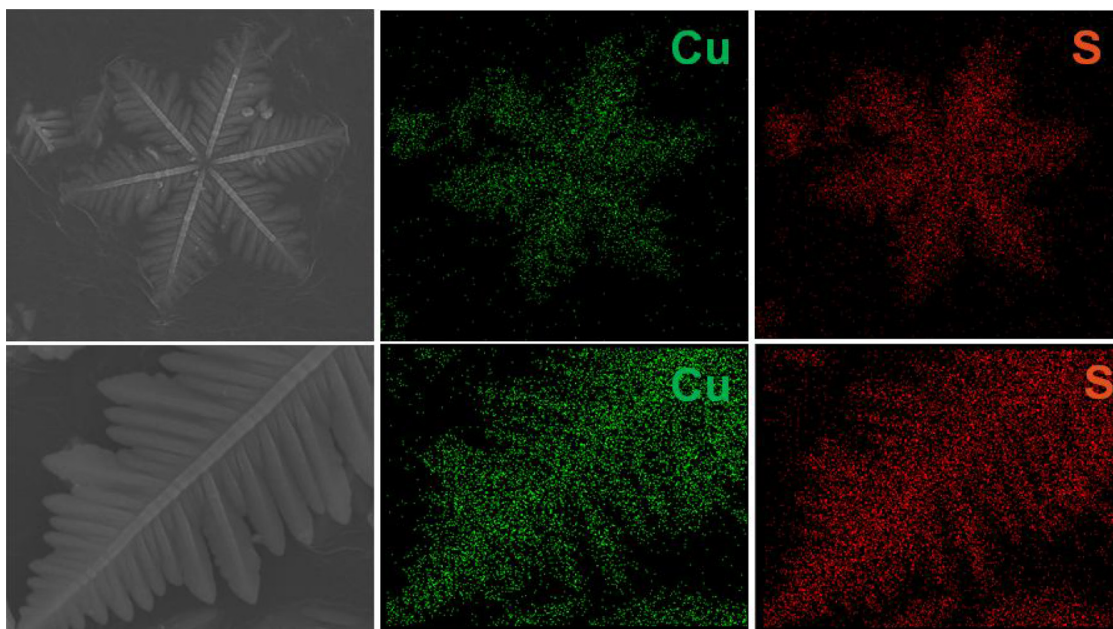
Fig. 2. Energy-dispersive X-ray spectroscopy (EDS) mapping of Cu₂S SFs.

Fig. 5 displays the SEM images of MoS₂ NS/Cu₂S SF composites with different MoS₂ loading amounts. As shown in Fig. 5a and c, for MoS₂ NS/Cu₂S SF composites (30 wt% MoS₂), a layer of nanoparticles are assembled onto the surface of Cu₂S SFs. The SEM images (Fig. 5b and d) of MoS₂ NS/Cu₂S SF composites (50 wt% MoS₂) highlight that with an appropriate loading amount of the MoS₂ precursors, the few-layered MoS₂ flakes cover on the surface of the Cu₂S SFs, which have obvious ripples and corrugations can be observed in the SEM images, suggesting the ultrathin nature of the MoS₂ NSs. For MoS₂ NS/Cu₂S SF composites (70 wt% MoS₂), the amount of MoS₂ precursors is critical as they are very likely to aggregate together by forming nanospheres (Fig. 5c and f), the same as pure MoS₂ NSs (Fig. S2), which will suppress photocatalytic activity of the catalysts. In addition, the energy dispersive X-ray spectrometry (EDS) mapping images (Fig. S3) of MoS₂ NS/Cu₂S SF composites (50 wt% MoS₂) clearly show the uniform distribution of individual elements of Cu, S and Mo, further confirming that the MoS₂ NSs are uniformly assembled on the surface of the Cu₂S SFs.

The morphology and microscopic structure of MoS₂ NS /Cu₂S SF composites have been further elucidated by TEM analysis. As shown in Fig. 6a, after assembling MoS₂ NSs on the surface of the Cu₂S SFs, the MoS₂ NS/Cu₂S SF composites still maintain snowflake structure. MoS₂ NSs with a very thin layer could be observed on the surface of the Cu₂S SFs, which can be seen in Fig. 6b and c. The high-resolution TEM images of MoS₂ NS/Cu₂S SF composites shown in Fig. 6d reveal the

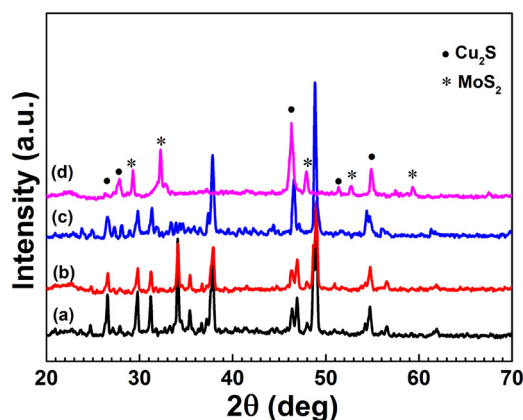**Fig. 4.** XRD patterns of Cu₂S architectures: (a) 60 °C (dendrites), (b) 80 °C (snowflakes), (c) 100 °C (sheets) and (d) MoS₂ NS/Cu₂S SF composites (50 wt% MoS₂).

interplanar spacing of 0.189 and 0.640 nm, which correspond to the (573) crystal planes of orthorhombic Cu₂S and the (002) crystal planes of hexagonal MoS₂, respectively [27,34]. These results also confirm that the heterostructures are well-formed between the Cu₂S SFs and the
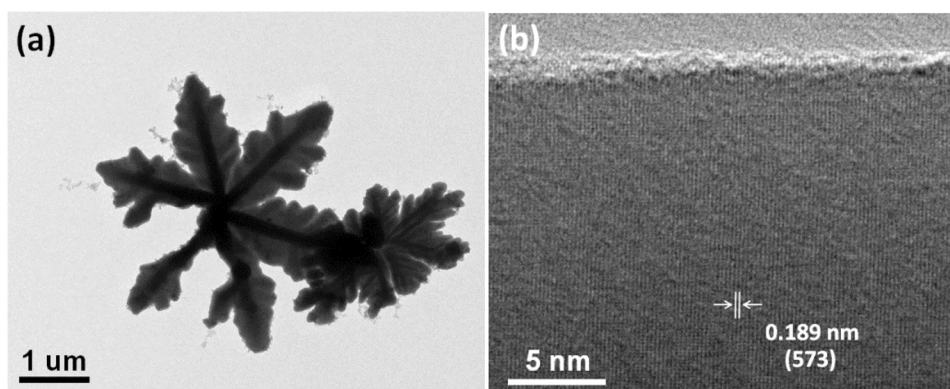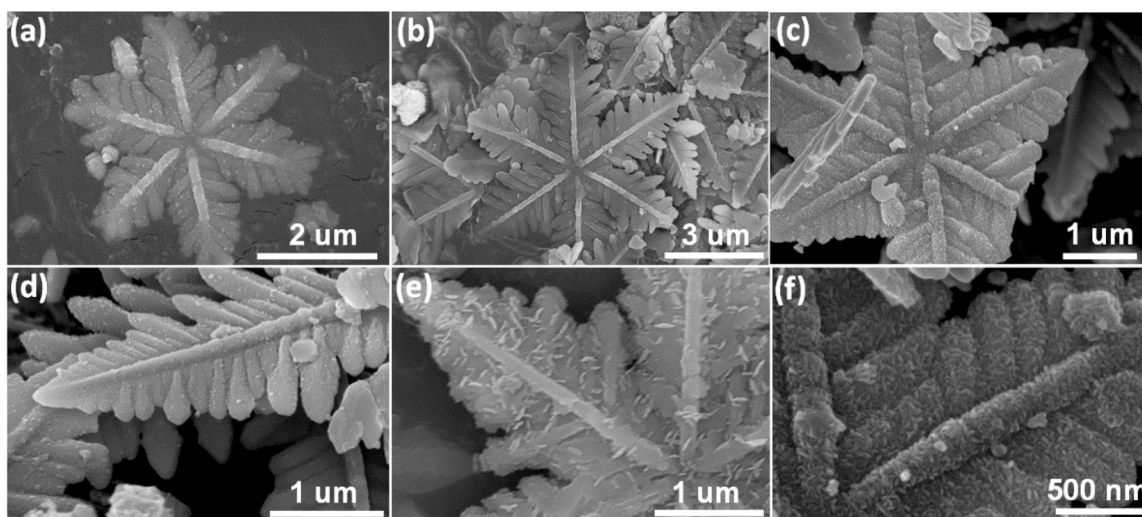

Fig. 3. TEM images of Cu₂S SFs.

Fig. 5. SEM images of MoS$_2$ NS/Cu$_2$S SF composites with different MoS$_2$ loading amounts: (a, d) 30 wt% MoS$_2$, (b, e) 50 wt% MoS$_2$, (c, f) 70 wt% MoS$_2$.

MoS$_2$ NSs. The as-fabricated heterostructure has faster charge separation and more efficient carrier transfer compared with pure Cu$_2$S SFs or MoS$_2$ NSs, and hence, the photocatalytic activities are improved.

XPS was used to investigate the surface elemental composition and elemental valences of MoS$_2$ NS/Cu$_2$S SF composites (Fig. 7 and S4). In the survey spectra for MoS$_2$ NS/Cu$_2$S SF composites (Fig. S4), all elements, namely Cu, Mo and S, are detected with strong characteristic peaks; no impurities are detected. The Cu 2p spectrum in Fig. 7a shows doublet peaks with binding energies of 932.6 and 952.7 eV, and can be identified as Cu 2p$_{3/2}$ and Cu 2p$_{1/2}$ lines of Cu$^+$, respectively [36]. Auger Cu LMM spectra of MoS$_2$ NS/Cu$_2$S SF composites (50 wt% MoS$_2$) was also collected to identify the valence of Cu (Fig. S5). Significantly, the associated Auger line (Cu LMM) at 569.6 eV indicated that Cu ion was in the form of Cu$^+$, which was the typical value for Cu$_2$S [14]. The S 2p XPS exhibited two sharp peaks at binding energies of 162.4 eV (2p$_{1/2}$) and 161.2 eV (2p$_{2/2}$) (Fig. 7b), which were characteristics of S^{2-} [34]. Two peaks which are located at 232.4 and 229.2 eV (Fig. 7c) can be ascribed to Mo 3d$_{3/2}$ and Mo 3d$_{5/2}$, respectively, revealing that
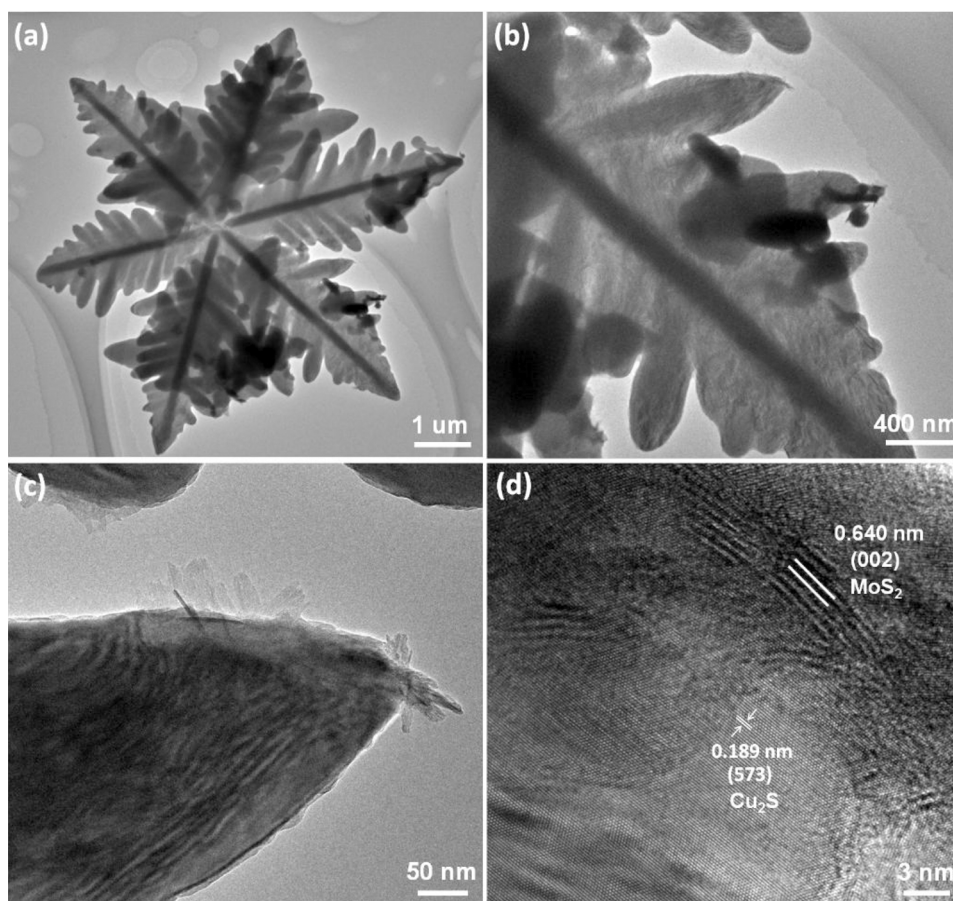

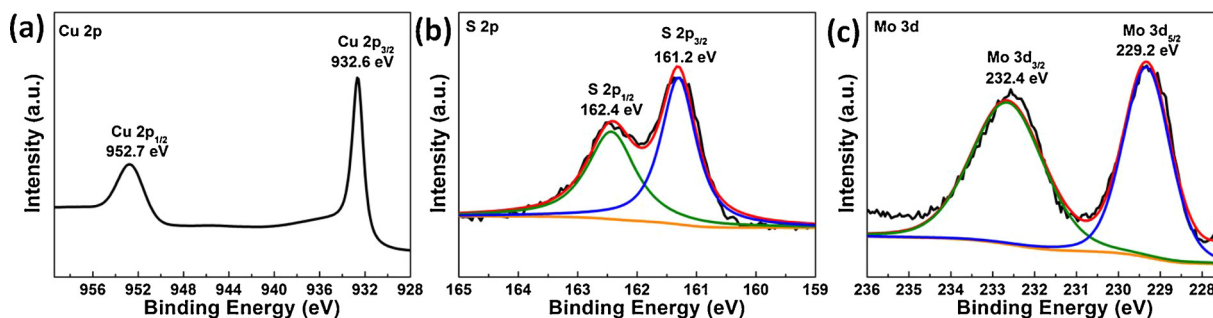**Fig. 6.** TEM images of MoS$_2$ NS/Cu$_2$S SF composites (50 wt% MoS$_2$).

Fig. 7. High resolution X-ray photoelectron spectra of elemental (a) Cu 2p, (b) S 2p and (c) Mo 3d in MoS$_2$ NS/Cu$_2$S SF composites (50 wt% MoS$_2$).
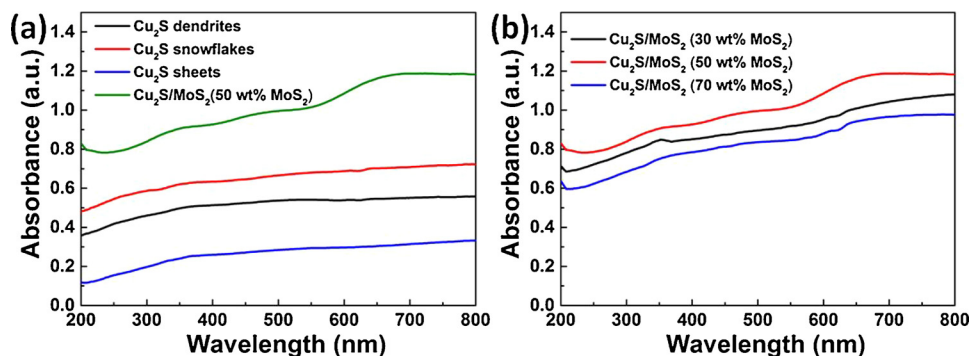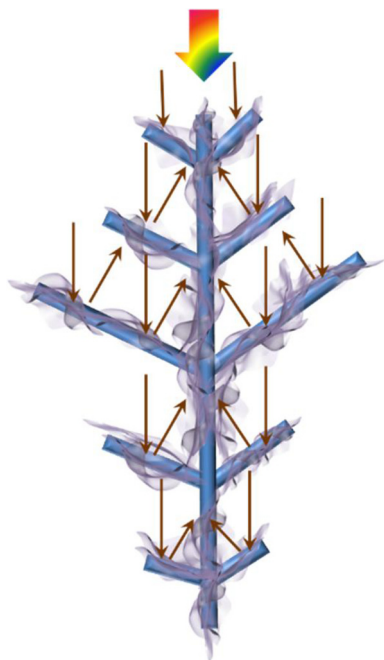

Fig. 8. UV–vis diffuse reflectance spectra of (a) Cu$_2$S architectures (dendrites, snowflakes and sheets) and (b) MoS$_2$ NS/Cu$_2$S SF composites (30 wt%, 50 wt% and 70 wt% MoS$_2$).

Scheme 2. Schematic illustrations of light reflecting and scattering within the simplified network of MoS$_2$ NS/Cu$_2$S SF composite.

Mo^{4+} is the dominant oxidation state [27].

3.2. Optical properties

UV–vis spectroscopy was applied to investigate the optical properties of the as-synthesized Cu$_2$S SFs, MoS$_2$ NSs, and MoS$_2$ NS/Cu$_2$S SF composites. Fig. 8 shows the UV–vis diffuse reflectance spectra (DRS) of the samples. The UV–vis DRS spectra of Cu$_2$S (Fig. 8a) show a broader light absorption in the visible region. As for Cu$_2$S synthesized under various reaction temperatures, the snowflakes (80 °C) have a higher absorbance capability than the dendrites (60 °C) and sheets (100 °C), which favor fully utilizing visible light for the irradiation of charge carriers. After MoS$_2$ NSs deposition, all of the MoS$_2$ NS/Cu$_2$S SF composites with different MoS$_2$ loading amounts exhibit a broader absorption region than that of Cu$_2$S SFs (Fig. 8a and b), which mainly due to the reason that the former can make better use of the sunlight. First of all, light would be reflected much more times among the branches and the multiple reflections would extend the light propagation path, which is beneficial to the full utilization of incident light. Second, MoS$_2$ NSs on the snowflake's surface can improve the light utilization efficiency by reflect unabsorbed light back to snowflake, which is beneficial to the full utilization of incident light.

As shown in Fig. 8b, the optimal MoS$_2$ loading amount is 50 wt%. The MoS$_2$ NS/Cu$_2$S SF composites (30 wt%) exhibit lower light absorption due to the less amount of visible light responsive MoS$_2$. Besides, the MoS$_2$ NS/Cu$_2$S SF composites (50 wt%) present better light absorption than that of MoS$_2$ NS/Cu$_2$S SF composites (70 wt%). This should be caused that excessive MoS$_2$ aggregate together by forming nanospheres, hinder the multiple reflections of light.

The UV–vis DRS spectra results (Fig. 8) indicate that the further increased optical absorption can be owed to a better light trapping properties and reflectance capability of the well-developed MoS$_2$ NS/Cu$_2$S SF composite in the whole visible region. Such regular snowflake-like structure with lush branches enables maximizing reflections and scatter efficiency, and thus resulting in multiple absorption of the incident light within the MoS$_2$ NS/Cu$_2$S SF composites. Herein we propose the possible reflecting and absorbing of light in a simplified pattern of MoS$_2$ NS/Cu$_2$S SF composite (Scheme 2). It is easy to see that when the light is shined into the lush branches of Cu$_2$S and wrinkles space of MoS$_2$, it bounces back and forth multiple times and finally be absorbed eventually. This is conducive to more effective photon capturing and thus resulting in an enhancement of light-harvesting efficiency. As show in Fig. S6, under the same MoS$_2$ loading amount (50 wt
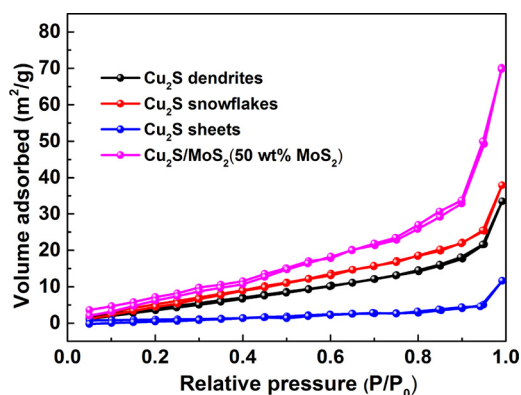
Fig. 9. Nitrogen adsorption-desorption isotherms of Cu_2S architectures (dendrites, snowflakes and sheets) and MoS_2 NS/Cu_2S SF composites (50 wt% MoS_2).

%), MoS_2 NS/Cu_2S SF composites have stronger light absorption than that of MoS_2 NS/Cu_2S dendrite composites and MoS_2 NS/Cu_2S sheet composites, which further prove the advantage of the structure of MoS_2 NS/Cu_2S SF composite. This phenomenon suggests that the MoS_2 NS/ Cu_2S SF composite has a potential photocatalytic activity under irradiation of visible light.

N_2 adsorption-desorption measurements were conducted to determine the specific surface area and porous structure of the as-obtained samples. The specific surface area is a significant property to investigate the photocatalytic activity of catalyst. Normally, lager specific surface area will lead to higher photocatalytic activity, because larger surface area can supply more active sites. As shown in Fig. 9, the nitrogen absorption isotherms display exhibits a typical type IV adsorption-desorption isotherm with a H3 hysteresis, which is the characteristic of mesoporous structure and slit-like pores. The specific surface area of Cu_2S dendrites, snowflakes, sheets, and MoS_2 NS/Cu_2S SF composites is 20.430, 28.173, 3.510, 60.512 $m^2\,g^{-1}$, respectively (Table S1). In addition, the corresponding pore size distribution plots shown in the Fig. S7 indicates that the average pore diameters of all the samples are a few tens nanometers. The specific surface area and pore volume value of the samples are listed in Table S1. The above results show that MoS_2 NS/ Cu_2S SF composite possesses much higher surface area and larger pore volume than other samples, which are attributed that nano-shaped MoS_2 NSs grow on the out surface of Cu_2S SFs, as proved by SEM (Fig. 5). The high specific surface area and large pore volume of MoS_2 NS/Cu_2S SF composites are beneficial for the adsorption and transfer of the pollutants and water in photocatalytic applications.

3.3. Photocatalytic degradation performance

In this study, the photocatalytic performance of the Cu_2S architectures under various reaction temperatures and MoS_2 NS/Cu_2S SF composites with different MoS_2 loading amounts has been evaluated toward photocatalytic degradation of methyl orange (MO) under visible light irradiation, as expressed in Fig. 10. The photolysis result without photocatalyst was also performed and shows that the dye solution is light-stable in the absence of photocatalyst (Fig. S8). Before light irradiation, dark adsorption experiment is done to ensure adsorption equilibrium of MO on the catalyst surface. No decomposition of MO is observed in the presence of catalyst in dark condition, showing the importance of light irradiation (Fig. 10). Fig. 10 shows the comparative photocatalytic test under different conditions in terms of relative concentration (C/C_0) with irradiation time (t), where C_0 represent the initial concentration of MO; C denotes the concentration at a given reaction time "t".

As can be seen in Fig. 10a, the Cu_2S snowflakes have a higher photocatalytic activity (72.8%) than the Cu_2S dendrites (55.9%) and

Cu_2S sheets (35.1%) after 60 min visible light irradiation. Three important factors were mainly considered. First, UV–vis light diffuse reflection spectra (UV–vis DRS) (Fig. 8) show that the snowflakes have a higher absorbance capability than the dendrites and sheets, which favors fully utilizing visible light for the irradiation of charge carriers. Second, the BET area of snowflakes is 28.173 $m^2\,g^{-1}$, which are higher than that of the dendrites (20.430 $m^2\,g^{-1}$) and sheets (3.510 $m^2\,g^{-1}$) (Table S1). Remarkably, more than 95% of MO are decomposed with MoS_2 NS/Cu_2S SF composites (50 wt% MoS_2) as the photocatalysts upon 60 min visible light irradiation. All of the MoS_2 NS/Cu_2S SF composites at different MoS_2 loading amounts present better photocatalytic properties than pure Cu_2S (Fig. 10a and b), indicate that the introduction of the MoS_2 component into the matrix of Cu_2S SFs gives rise to an obvious visible photoactivity improvement toward the degradation of MO. The reason may be attributed to the following three points: (1) It has been demonstrated that the snowflake-like structure maximize light-harvesting efficiency, originating from the well-developed snowflake-like structure with lush branches; (2) the Cu_2S SFs can provide a matrix to suppress the aggregation of MoS_2 NSs; (3) Compared with pure Cu_2S SFs or MoS_2 NSs, the MoS_2 NS/Cu_2S SF composites have a larger specific surface area (Table S1), which can supply more surface active sites and promote charge-carrier transport, favoring enhanced photocatalytic activity; (4) The formed heterojunction between Cu_2S and MoS_2 can provide much more direct electron transit pathway for efficient electron transport to suppress the charge recombination.

The MoS_2 loading amounts exercises a great influence on the activities of MoS_2 NS/Cu_2S SF composites in the visible, as shown in Fig. 10b. The optimal MoS_2 loading amounts is 50 wt% MoS_2. The MoS_2 NS/Cu_2S SF composites at lower MoS_2 loading amounts (30 wt% MoS_2) exhibit lower photocatalytic efficiency due to too little MoS_2 resulting in a failure of lightharvesting augmentation, which will depress the photocatalytic activities. Besides, the MoS_2 NS/Cu_2S SF composites (50 wt% MoS_2) present better photocatalytic properties than that of MoS_2 NS/Cu_2S SF composites (70 wt% MoS_2). This should be caused that excessive MoS_2 cover the active sites of Cu_2S SFs, which hinder the electron transfer on the interface of MoS_2 NS/Cu_2S SF composites, and thus in turn inhibit the photoactivity Hence, only a suitable MoS_2 loading amounts can realize the best photocatalytic outcome. Meanwhile, the total organic carbon (TOC) removal rate of MoS_2 NS/Cu_2S SF composites (50 wt% MoS_2) for degradation of MO is shown in Fig. S9. It can be seen that the removal rate of TOC reaches to 90% after 60 min of visible light exposure, demonstrating that MO molecules and its derivatives can be effectively removed by photocatalysis. To discriminate real visible photocatalytic activity, photocatalytic experiments employing other typical organic dyes, *e.g.*, rhodamine B and methyl blue, have also been performed to assess real visible photocatalytic performance of the as-prepared MoS_2 NS/Cu_2S SF composite (Fig. S10).

To investigate the reaction kinetics of MO degradation, the experimental data are analyzed by the pseudo-first-order kinetic model. $-\ln (C/C_0) = kt$, where k (min^{-1}) is the rate constant. The reaction rate constants k of Cu_2S SFs under various reaction temperatures and MoS_2 NS/Cu_2S SF composites removal are shown in Table S2. Fig. 11a and b shows the reaction kinetic curves for the samples of Cu_2S dendrites, snowflakes, sheets, and MoS_2 NS/Cu_2S SF composites with different MoS_2 loading amounts: 30 wt%, 50 wt%, 70 wt% MoS_2, of which apparent reaction kinetic constants are calculated to be $8.2*10^{-3}$, $22.1*10^{-3}$, $15.3*10^{-3}$, $34.1*10^{-3}$, $50.1*10^{-3}$ and $25.1*10^{-3}\,min^{-1}$ under visible light irradiation, respectively. Thus, the reaction rate by MoS_2 NS/Cu_2S SF composites is faster than that of pure Cu_2S. The variation of the rate constants is consistent with the variation in photocatalytic activity (Fig. 10). Thus, it could regard as a green and energy-saving method using MoS_2 NS/Cu_2S SF composites for environmental cleaning. And the mechanism would be explained in detail in the mechanism section.

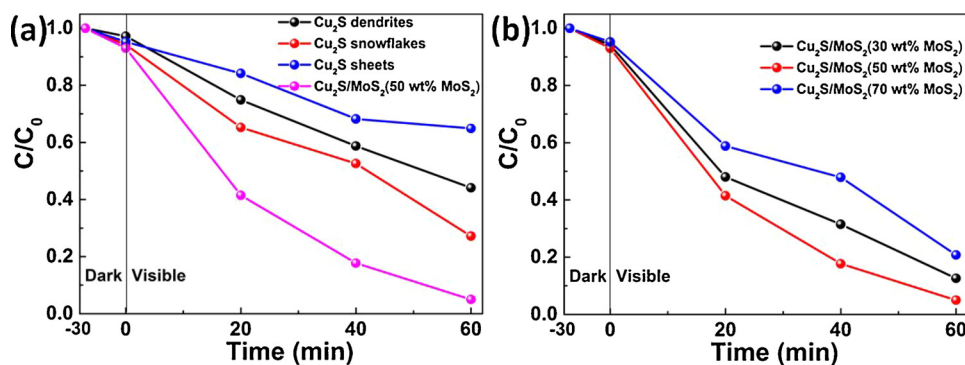The stability and reusability of MoS_2 NS/Cu_2S SF composites were

Fig. 10. Photocatalytic decomposing of MO in the presence of (a) Cu_2S architectures (dendrites, snowflakes and sheets) and (b) MoS_2 NS/Cu_2S SF composites (30 wt %, 50 wt% and 70 wt% MoS_2) under visible light irradiation.

also tested (Fig. 12). There is no obvious change after ten cycles, almost 88% of MO are decomposed, suggesting good durability of such a MoS_2 NS/Cu_2S SF composite catalyst. The SEM image and XRD pattern confirm the well maintenance of the morphology and crystallographic form of MoS_2 NS/Cu_2S SF samples after long time cycling (Fig. S11). The results indicated that MoS_2 NS/Cu_2S SF composite was stable and resistant to photocorrosion in the photocatalytic process.

3.4. Electron transfer mechanism

To evaluate the effect of the active species (h^+, $\cdot OH$, or $\cdot O_2^-$) involved in the catalytic degradation process, radical trapping experiments were performed under visible light illumination (Fig. 13). EDTA (10 mM), methanol (1: 15/V: V), and benzoquinone (1 mM) were used as h^+, $\cdot OH$, and $\cdot O_2^-$, respectively. The addition of EDTA (a trapper of h^+) and benzoquinone (a trapper of $\cdot O_2^-$) inhibit the degradation of MO almost completely. This result indicates that h^+ and $\cdot O_2^-$ radicals are the primary oxidation species in this photocatalytic system. While, in the case of the presence of methanol (a trapper of $\cdot OH$), the degradation rate of MO changes little compared to that without any scavengers, indicating that $\cdot OH$ does not play a role on this photocatalytic process.

As we can see from Scheme 2, light would be reflected much more times among the branches of the MoS_2 NS/Cu_2S SF composite structure than that of MoS_2 NS structure and the multiple reflections would extend the light propagation path, which is beneficial to the full utilization of incident light. The charge transfer processes and various energy gap structures of the samples obtained were exhibited in Scheme 3. The conduction band (CB)/valence band (VB) potentials of Cu_2S and MoS_2 are $^-0.06/+1.14$ and $+0.4/+2.27$ eV vs NHE, respectively [37,38]. As shown in Scheme 3, under light irradiation, electrons and holes are generated in both Cu_2S and MoS_2. MoS_2 is combined with Cu_2S in the
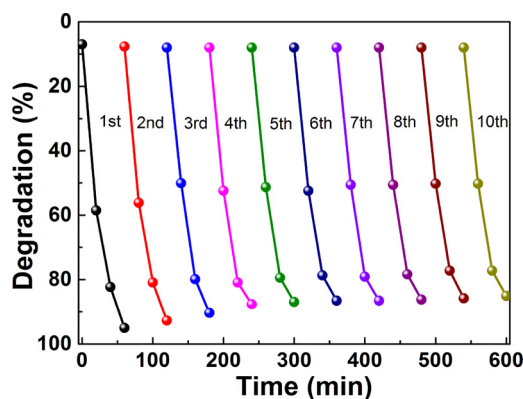

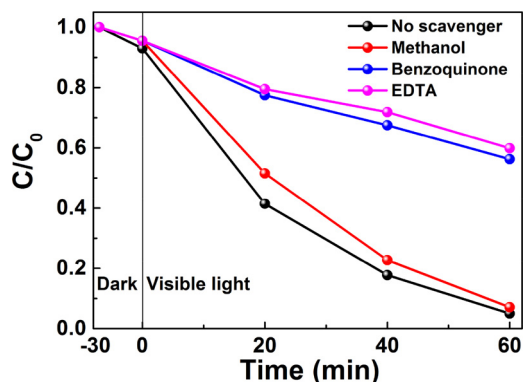**Fig. 12.** Photocatalytic degradation of MO for MoS_2 NS/Cu_2S SF composites (50 wt% MoS_2) under visible light irradiation.

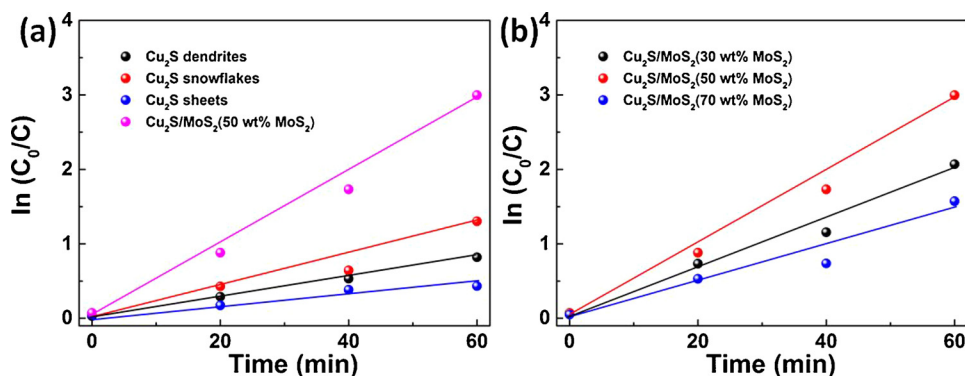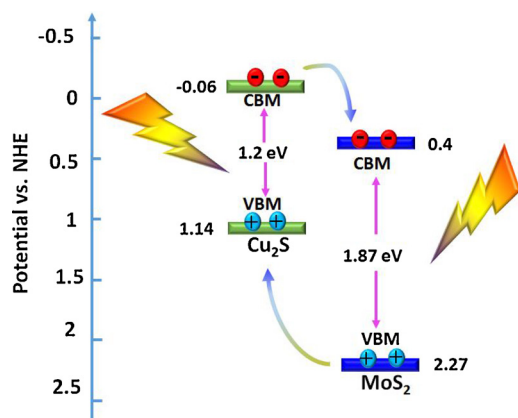**Fig. 13.** Active species trapping experiments of MoS_2 NS/Cu_2S SF composites.

Fig. 11. Kinetic plots of MO in the presence of (a) Cu_2S architectures (dendrites, snowflakes and sheets) and (b) MoS_2 NS/Cu_2S SF composites (30 wt%, 50 wt% and 70 wt% MoS_2) under visible light irradiation.

Scheme 3. Diagram of type-II band alignment mechanism of MoS_2 NS/Cu_2S SF composites under visible light irradiation.

form of heterojunction, in which the electrons can transfer from the CB of the Cu_2S to that of the MoS_2, contrarily, the holes immigrate from the VB of the MoS_2 to that of the Cu_2S. So the photo-induced electrons and holes have been effectively separated in the composite structure, which decreases the recombining ratio of photo-induced electrons and holes [39]. The VB potential of MoS_2 (2.27 *vs* NHE) does not meet the requirements of the generation of ·OH (2.4 *vs* NHE) [40], thus pollutants can be mainly removed by h^+ and $·O_2^-$.

3.5. Photocatalytic H_2 production performance

In order to illuminate superior catalytic properties and potential applications of as-synthesized MoS_2 NS/Cu_2S SF composites, they were composited with TiO_2 nanoparticles and the photocatalytic H_2 production performance was evaluated under Xe lamp irradiation for 3 h (Fig. 14). As can be seen in Fig. 14a, bare TiO_2 has almost no photocatalytic activity due to the high recombination rate of the photogenerated electrons and holes at the surface of the TiO_2. When Cu_2S combined with TiO_2, The experimental result (Fig. 14a) shows that the photocatalytic H_2 production rate of dendritic and sheet Cu_2S decorated with TiO_2 is 463.8 and 152.7 μ mol/g, respectively, while the snowflake Cu_2S is 752.1 μ mol/g, having a higher photocatalytic activity for H_2 production. Because snowflake-like Cu_2S has a higher specific surface area and possesses more surface active sites and photocatalytic reaction centers, it exhibits a better photocatalytic performance to produce H_2. Among all the photocatalysts, MoS_2/Cu_2S-TiO_2 exhibits a remarkable hydrogen production activity of average 1567.1 μmol/g, which is about 10-times higher than that of sheet Cu_2S-TiO_2. For comparison, we carried out the H_2 generation activity of metal (Pt)-TiO_2 without MoS_2/Cu_2S or Cu_2S. As shown in Fig. 14a, the amount of H_2 generation in the MoS_2/Cu_2S-TiO_2 photocatalyst is slightly higher than that of the metal-

TiO_2 photocatalyst. We also measured the hydrogen evolution of MoS_2/Cu_2S-TiO_2 and Pt-TiO_2 under UV and visible light (Fig. S12). As expected, under UV light irradiation, the hydrogen evolution over Pt-TiO_2 is higher than that of MoS_2/Cu_2S-TiO_2. However, under visible light irradiation, the Pt-TiO_2 almost has no H_2 generation activity due to the wide bandgap of TiO_2. MoS_2/Cu_2S-TiO_2 exhibits an enhanced hydrogen production activity of 602.1 μmol/g. The high H_2 production activity of MoS_2/Cu_2S-TiO_2 can be attributed to the following: (i) the formation of an effective and efficient heterojunction between TiO_2 and MoS_2/Cu_2S, which leads to rapid and effective charge transport and separation of the photogenerated e^-/h^+ pairs [41,42]; (ii) the introduction of MoS_2/Cu_2S inducing enhanced light absorption over the visible region; and (iii) the enhanced active MoS_2 edge sites which adsorb and stabilize H^+ and facilitate H_2 production. At the same time, MoS_2/Cu_2S-TiO_2 displayed a stable photocatalytic activity for H_2 production (Fig. 14b). The above results clearly illustrate the significantly enhanced photocatalytic H_2 production activity of the hybrid MoS_2/Cu_2S-TiO_2 structure.

4. Conclusions

In summary, we have developed an innovative method to acquire Cu_2S with novel snowflake-like morphologies. The research demonstrated that thiourea as the precursor of sulfur and EDA as the solvent were the key template for the formation of snowflake-like structures. Then MoS_2 NSs are assembled onto the surface Cu_2S SFs to construct the MoS_2 NS/Cu_2S SF composites. The primary photocatalytic tests confirm that the as-obtained MoS_2 NS/Cu_2S SF composite possess robust photocatalytic properties for MO degradation and H_2 production as cocatalysts. The results show that the significantly improved photocatalytic activity is a direct consequence of high light-harvesting efficiency due to the snowflake structure and the relatively high surface area, as well as the charge separation of the photogenerated carriers caused by the heterojunction between MoS_2 and Cu_2S. Moreover, it provides some new insights into the design and fabrication of advanced photocatalytic materials with complex architectures for high efficiency in solar energy conversion.
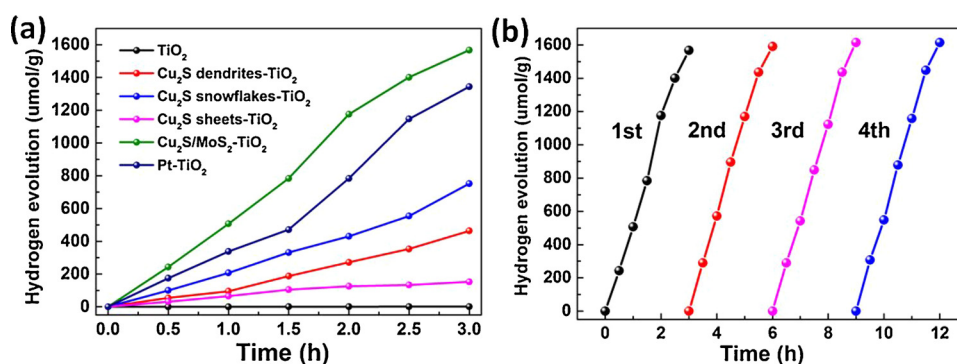
Fig. 14. Hydrogen generation as a function of time with Cu_2S dendrites-TiO_2, Cu_2S snowflakes-TiO_2, Cu_2S sheets-TiO_2, MoS_2/Cu_2S (50 wt% MoS_2)-TiO_2, metal-TiO_2, and bare TiO_2 samples under irradiation of UV–vis light; (b) Recycle hydrogen generation of MoS_2/Cu_2S (50 wt% MoS_2)-TiO_2 measured after each interval of 3 h.

Appendix A. Supplementary data

Supplementary material related to this article can be found, in the online version, at doi:https://doi.org/10.1016/j.apcatb.2018.03.074.

References

[1] X. Hao, Z. Jin, H. Yang, G. Lu, Y. Bi, Appl. Catal. B Environ. 210 (2017) 45–56.
[2] X. Hu, Y. Li, J. Tian, H. Yang, H. Cui, J. Ind. Eng. Chem. 45 (2017) 189–196.
[3] Z. Jin, X. Zhang, Y. Li, S. Li, G. Lu, Catal. Commun. 8 (2007) 1267–1273.
[4] Z. Su, H. Li, P. Chen, S. Hu, Y. Yan, Catal. Sci. Technol. 7 (2017) 5105–5112.
[5] X. Hu, X. Liu, J. Tian, Y. Li, H. Cui, Catal. Sci. Technol. 7 (2017) 4193–4205.
[6] Y. Chen, C.H. Chuang, Z. Qin, S. Shen, T. Doane, C. Burda, Nanotechnology 28 (2017) 084002.
[7] J. Zhang, X. Ma, L. Zhang, Z. Lu, E. Zhang, H. Wang, Z. Kong, J. Xi, Z. Ji, J. Phys. Chem. C 121 (2017) 6133–6140.
[8] J. Tian, X. Hu, N. Wei, Y. Zhou, X. Xu, H. Cui, H. Liu, Sol. Energy Mat. Sol. Cells 151 (2016) 7–13.
[9] Z. Jin, X. Zhang, G. Lu, S. Li, J. Mol. Catal. A Chem. 259 (2006) 275–280.
[10] W. Jiang, S. Bai, L. Wang, X. Wang, L. Yang, Y. Li, D. Liu, X. Wang, Z. Li, J. Jiang, Small 12 (2016) 1640–1648.
[11] D. Liu, Z. Jin, Y. Bi, Catal. Sci. Technol. 7 (2017) 4478–4488.
[12] A. Tanaka, K. Teramura, S. Hosokawa, H. Kominami, T. Tanaka, Chem. Sci. 8 (2017) 2574–2580.
[13] C.P. Sajan, S. Wageh, A.A. Al-Ghamdi, J. Yu, S. Cao, Nano Res. 9 (2016) 3–27.
[14] M. Ye, C. Chen, N. Zhang, X. Wen, W. Guo, C. Lin, Adv. Energy Mater. 4 (2014) 1301564.
[15] L. An, P. Zhou, J. Yin, H. Liu, F. Chen, H. Liu, Y. Du, P. Xi, Inorg. Chem. 54 (2015) 3281–3289.
[16] B. Li, L. Huang, G. Zhao, Z. Wei, H. Dong, W. Hu, L.W. Wang, J. Li, Adv. Mater. 28 (2016) 8271–8276.
[17] A.B. Wong, S. Brittman, Y. Yu, N.P. Dasgupta, P. Yang, Nano Lett. 15 (2015) 4096–4101.
[18] C. Rohner, A. Pekkari, H. Härelind, K. Moth-Poulsen, Langmuir 33 (2017) 13272–13276.
[19] Y. Wang, L. Liu, Q. Wang, S. Hu, P. Zou, J. Shi, X. Zhang, Nanotechnology 27 (2015) 015705.
[20] M. Ye, C. Chen, N. Zhang, X. Wen, W. Guo, C. Lin, Adv. Energy Mater. 4 (2014) 1079–1098.
[21] Q. Zhang, H. Tian, N. Li, M. Chen, F. Teng, CrystEngComm 16 (2014) 8334–8339.
[22] Y. Xia, X. Pu, J. Liu, J. Liang, P. Liu, X. Li, X. Yu, J. Mater. Chem. A 2 (2014) 6796–6800.
[23] B. Yan, Y. Wang, T. Jiang, X. Wu, J. Mater. Sci. Mater. Electron. 27 (2016) 4035–4042.
[24] M.M. Khan, S.A. Ansari, D. Pradhan, M.O. Ansari, J. Lee, M.H. Cho, J. Mater. Chem. A 2 (2014) 637–644.
[25] K. He, C.Y. Xu, L. Zhen, W.Z. Shao, Mater. Lett. 62 (2008) 739–742.
[26] Z. Xu, Y. Ben, Z.L. Chen, F. Qi, Mater. Res. Bull. 48 (2013) 1725–1727.
[27] X. Hu, H. Zhao, J. Tian, J. Gao, Y. Li, H. Cui, Sol. Energy Mat. Sol. Cells 172 (2017) 108–116.
[28] J. He, L. Chen, F. Wang, Y. Liu, P. Chen, C.T. Au, S.F. Yin, ChemSusChem 9 (2016) 624–630.
[29] L. Zheng, S. Han, H. Liu, P. Yu, X. Fang, Small 12 (2016) 1527–1536.
[30] M. Ben Ali, W.K. Jo, H. Elhouichet, R. Boukherroub, Int. J. Hydrogen Energy 42 (2017) 16449–16458.
[31] H. Li, K. Yu, Z. Tang, H. Fu, Z. Zhu, Phys. Chem. Chem. Phys. 18 (2016) 14074–14085.
[32] X. Zhang, Y. Yang, S. Ding, W. Que, Z. Zheng, Y. Du, Inorg. Mater. 56 (2017) 3386–3393.
[33] D.G.S. Quattrociocchi, M.V.M. Meuser, G.B. Ferreira, J.W.D.M. Carneiro, S.R. Stoyanov, L.M.D. Costa, J. Mol. Model. 23 (2017) 60.
[34] A.C. Poulose, S. Veeranarayanan, M.S. Mohamed, Y. Nagaoka, R. Romero Aburto, T. Mitcham, P.M. Ajayan, R.R. Bouchard, Y. Sakamoto, Y. Yoshida, T. Maekawa, D. Sakthi Kumar, Nanoscale 7 (2015) 8378–8388.
[35] Y.B. Chen, L. Chen, L.M. Wu, Chem. Eur. J. 14 (2008) 11069–11075.
[36] Y.J. Lu, J.H. Jia, Chin. Chem. Lett. 25 (2014) 1473–1478.
[37] B. Wang, W. An, L. Liu, W. Chen, Y. Liang, W. Cui, RSC Adv. 5 (2015) 3224–3231.
[38] Y. Liu, Y.X. Yu, W.D. Zhang, J. Phys. Chem. C 117 (2013) 12949–12957.
[39] J. Tian, P. Hao, N. Wei, H. Cui, H. Liu, ACS Catal. 5 (2015) 4530–4536.
[40] W.K. Jo, J.Y. Lee, T.S. Natarajan, Phys. Chem. Chem. Phys. 18 (2016) 1000–1016.
[41] H. Li, Z. Su, S. Hu, Y. Yan, Appl. Catal. B Environ. 207 (2017) 134–142.
[42] K. Fan, Z. Jin, H. Yuan, H. Hu, Y. Bi, Chin. J. Catal. 38 (2017) 2056–2066.